Variable-Stiffness Nasotracheal Intubation Robot with Passive Buffering: A Modular Platform in Mannequin Studies

Ruoyi Hao, Jiewen Lai, Wenqi Zhong, Dihong Xie, Yu Tian, Tao Zhang, Yang Zhang,
Catherine P. L. Chan, Jason Y. K. Chan, and Hongliang Ren

***Abstract*— Intubation is a critical medical procedure for securing airway patency in patients, but the inconsistent skill levels among medical practitioners necessitate the advancement of better robotic solutions. While orotracheal intubation robots have been widely developed, nasotracheal intubation remains essential in specific clinical scenarios. However, nasotracheal intubation robots are still underdeveloped and lack buffer protection mechanisms to ensure safety. This study presents a novel variable-stiffness nasotracheal intubation robot (NIR) with passive buffering. The proposed NIR is a modular platform capable of performing the main steps of nasotracheal intubation, validated through mannequin studies via teleoperation. We proposed a variable-stiffness fiberoptic bronchoscope (FOB) control module for the FOB distal end control, and validated its dual functionality in experiments: low-stiffness mode provides passive buffering during nasal cavity navigation, with a frontal peak force of 2.8 N and a lateral peak force of 0.12 N; high-stiffness mode enhances load-bearing capacity for near-glottis navigation, with a frontal bearing force of 4.9 N and a lateral bearing force of 0.42 N. Additionally, a compact (74 × 64 × 53 mm, 150 g) FOB feeding module with passive failure protection was designed to limit the max frontal impact force to 2.3 N.**

I. INTRODUCTION

Mechanical ventilation and intubation are crucial for treating acute respiratory failure, upper airway obstruction, anesthesia, and other-induced respiratory muscle dysfunction [1], [2]. Over 20 million patients globally receive mechanical ventilation annually [3]. Intubation is a common and effective method. It establishes an artificial airway and facilitates mechanical ventilation by inserting an endotracheal tube or nasotracheal tube into the patient's airway [4]. However, intubation is a complex procedure that demands expert skill to ensure safety and efficacy, aiming for first-attempt success and minimal patient risk [5]. *First-pass success rates* vary significantly among healthcare providers [6], [7], which highlights the procedure's complexity and the impact of skill disparities. Notably, repeated attempts increase adverse events and complications, like inadvertent esophageal intubation [8], nasal and sinus injuries and laryngeal edema [9]. Besides, intubation exposes medical staff to viral and other infectious risks [10]. For example, the pandemic of COVID-19 reminds us of in-hospital respiratory cross-infection perils [11].

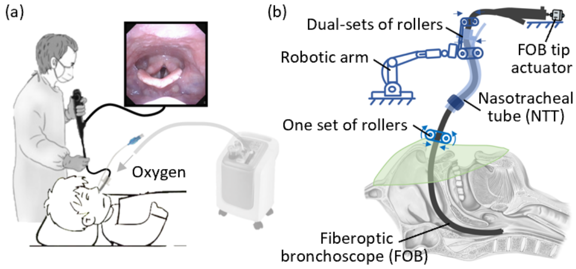

Fig. 1. Nasotracheal Intubation Procedure. (a) Current manual method. (b) Proposed robot-assisted approach.

Researchers have recently explored the medical application of robotic technology [12]–[15] for intubation procedures. Using the Da Vinci surgical system, Tighe *et al.* [16] demonstrated robot-assisted intubation on a simulation phantom, establishing the viability of robotic airway management. In the subsequent decade, extensive robot-assisted orotracheal intubation research has developed [17]–[23]. Lai *et al.* [24], [25] developed a portable steerable endoscope capable of automatic image-guided navigation from the mouth to the glottis, using a sim-to-real approach, facilitating orotracheal intubation. Orotracheal intubation robots have seen significant advancements, but research on nasotracheal intubation (NI) robots remains limited. Despite orotracheal intubation's widespread use, NI remains crucial for: 1) surgeries requiring an unobstructed oral cavity; 2) patients with limited mouth opening; 3) high-risk emergency cases needing awake intubation; 4) cases with restricted laryngoscopic view; and 5) prolonged intubation scenarios.

Given the importance of NI in specific clinical scenarios, recent efforts have begun to address these challenges. Deng *et al.* [26], [27] developed a master-slave robotic nasotracheal intubation system (RNIS) with 3-DOF endoscopic control, assisted teleoperation, and visual feedback. Simulator and phantom experiments tested the system's feasibility. To address the risk of esophageal intubation, they applied various advanced techniques to the endoscopic image [28]–[31], including monocular depth estimation, optical flow estimation, intensity estimation, and neural network-based segmentation. These methods aim to reduce collisions of the endoscope and assist in locating the glottis. However, RNIS was only developed for the first step, i.e., inserting the endoscope from the nose into the trachea, and the other steps of the NI procedure have not been completed. Moreover, its use of

---

This work is supported in part by the Hong Kong Research Grants Council (RGC) Collaborative Research Fund CRF-C4026-21G. *(Corresponding Author: Hongliang Ren)*.

R. Hao, J. Lai, D. Xie, Y. Tian, T, Zhang and H. Ren are with the Department of Electronic Engineering, The Chinese University of Hong Kong, Shatin, N.T., Hong Kong SAR, China. `hlren@ee.cuhk.edu.hk`

W. Zhong is with the Faculty of Applied Science, Macao Polytechnic University, Macau, China

Y. Zhang is with the School of Mechanical Engineering, Hubei University of Technology, Wuhan, China

C. P. L. Chan and Jason Y. K. Chan are with the Department of Otorhinolaryngology, Head and Neck Surgery, The Chinese University of Hong Kong, Hong Kong SAR, China

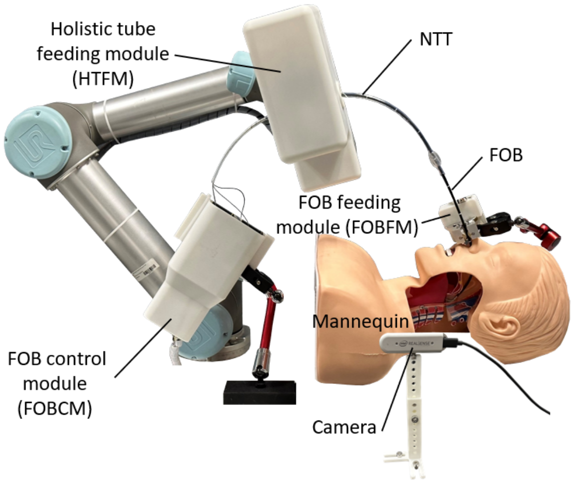

Fig. 2. The nasotracheal intubation robot (NIR) system comprises three custom modules, a robotic arm, and a camera. It achieves the nasotracheal intubation procedure by separately manipulating the FOB and NTT.

a screw mechanism to insert the endoscope raises concerns about the force interaction with human tissue.

Therefore, we identify the challenges, including 1) the lack of a robot capable of performing the main steps of NI; and 2) the need for multiple buffer protection mechanisms to ensure safety during human-robot interaction. To fill these gaps, in this paper, we propose a novel nasotracheal intubation robot (NIR) system with the following contributions:

- An extensible modular robotic platform capable of performing the 3 main steps of the NI procedure has been developed. Its feasibility has been validated in mannequin studies via teleoperation control.
- A variable-stiffness fiberoptic bronchoscope (FOB) control module has been proposed for controlling the FOB distal end. Experimental results have validated its dual functionality: low-stiffness mode for passive buffering used in nasal passage (frontal peak force: 2.8 N, lateral peak force: 0.12 N) and high-stiffness mode for load-bearing near-glottis navigation (frontal bearing force: 4.9 N, lateral bearing force: 0.42 N).
- A compact (74 × 64 × 53 mm, 150 g) FOB feeding module has been proposed and experimentally validated, demonstrating another effective protection through passive failure mechanisms, limiting the maximum frontal impact force to 2.3 N.

II. SYSTEM DESCRIPTION

For the current NI procedure shown in Fig. 1(a), we proposed a robot-assisted approach as shown in Fig. 1(b), and further developed to nasotracheal intubation robot (NIR), illustrated in Fig.2. The robot inserts the nasotracheal tube (NTT) through the nasal passage and upper respiratory tract into the trachea under the guidance of FOB. Once correctly positioned, it withdraws the FOB while maintaining the NTT in situ, thus establishing an artificial airway. This robotic system comprises a holistic tube feeding module (HTFM) mounted on the robotic arm's end-effector, an FOB feeding module, an FOB control module, and an external camera.

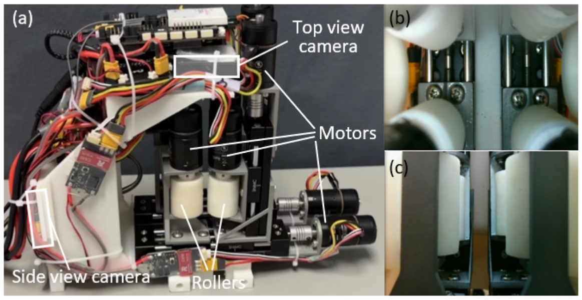

Fig. 3. Holistic tube feeding module. (a) Compact module prototype. (b) Top view camera perspective. (c) Side view camera perspective.

A. Holistic Tube Feeding Module (HTFM)

To tackle the unique challenge of manipulating two nested flexible tubular objects during intubation, we developed a holistic tube feeding module. As shown in Fig. 3, actuated by eight motors, the HTFM control the rotational and translational motions of four rollers via transmission parts, thus controlling the two manipulated objects' motion. It incorporates two internal cameras for real-time feedback from side and top views. An integrated low-level control system is encapsulated with the mechanical assembly in a compact casing, facilitating efficient mounting on the robotic arm's end-effector.

The FOB and NTT are appropriately manipulated by integrating coarse robotic arm adjustments and fine HTFM control. Based on the outside view, the robotic arm controls the approximate pose of the HTFM while maintaining collision avoidance. Based on inside views, the HTFM executes fine-tuned manipulations of the FOB and NTT, particularly during phases of patient interaction, offering enhanced safety compared to direct robotic arm operations.

B. Variable-Stiffness FOB Control Module (FOBCM)

To address the requirement for buffer protection mechanisms, we developed a variable-stiffness FOB control module to control the FOB distal end. As illustrated in Fig. 4, the mechanism comprises two identical tendon control modules, each responsible for manipulating one of the FOB tendons. Each module consists of a motor, a linear slide, a driver unit, a fixed unit, and a driven unit. The tendon sheath and tendon are secured to the driver and driven units, respectively, using drill chucks. Active adjustment of the distance between the driver and fixed units is achieved through a motor-driven leadscrew transmission. The driven unit is designed to traverse along the steel shaft of the linear slide via linear bearings, enabling smooth axial movement. Two coil springs and a displacement sensor are positioned between the fixed and driven units, facilitating passive adjustment of their relative distance in response to variations in tendon tension.

Fig. 5(a) presents a schematic representation of the force-tuning mechanism within a tendon control module. Designating the fixed unit's position as the reference, we define x_a as the distance between the driven unit and the fixed unit, corresponding to the spring length, with an initial value of x_{a0}. Similarly, x_b denotes the distance between the driver unit and the fixed unit, which is initially set to x_{b0}. In a simplified

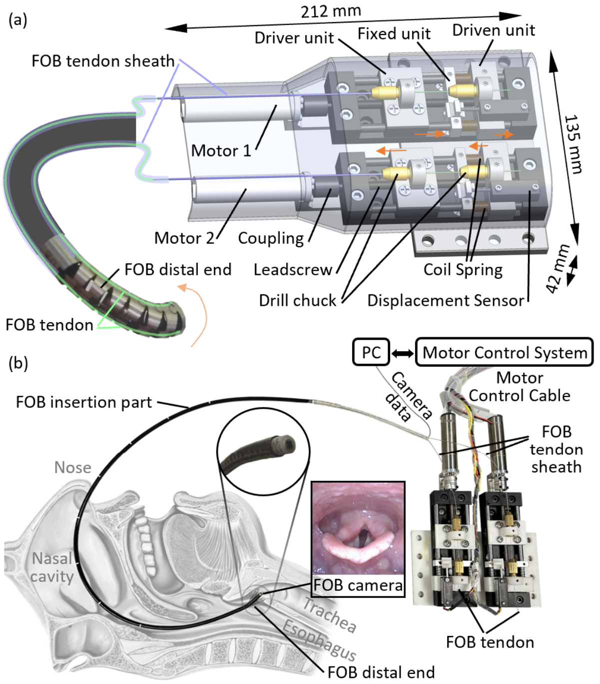

Fig. 4. Variable-stiffness FOB control module with passive adjustment of their relative distance in response to variations in tendon tension. (a) Mechanism design. (b) Prototype.

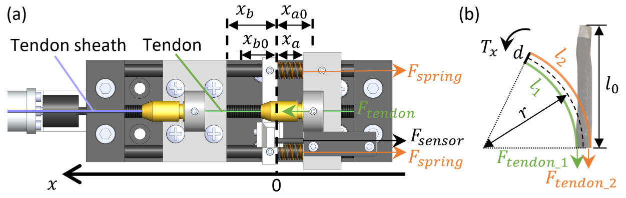

Fig. 5. Schematic of force tuning mechanism. (a) Tendon control module. (b) Two tendons in the FOB distal end.

analysis without frictional forces and dynamic effects, the tension force can be described using Hooke's law by

$$F_{tension} = \frac{E \cdot A \cdot \Delta L}{L}, \tag{1}$$

where E is the elastic modulus of the tendon wire, A is the cross-sectional area of the steel wire, L is the original length of the wire. $\Delta L = \Delta x_a + \Delta x_b + \Delta l$ is the differential length, where $\Delta x_a = x_a - x_{a0}$ is the differential displacement of the driven unit, and $\Delta x_b = x_b - x_{b0}$ denotes the differential displacement of the driver unit, which is driven by the motor through the rotation of the leadscrew, $\Delta l = l - l_0$ is the differential displacement of FOB tendon in the distal end. And l denotes the current length of the FOB tendon's distal end segment, and l_0 is its initial length.

Based on static equilibrium principles on the driven unit, the tension force can be decomposed as

$$F_{tension} = 2\underbrace{F_{spring}}_{-k_1 \Delta x_a} + \underbrace{F_{sensor}}_{-k_2 \Delta x_a}, \tag{2}$$

where F_{spring} denotes the recoil force generated by spring compression, and F_{sensor} represents the recoil force produced by displacement sensor compression. Both F_{spring} and F_{sensor} are related to Δx_a, and k_1 and k_2 are the elastic coefficients of the coil springs and displacement sensor, respectively. As such, we can obtain

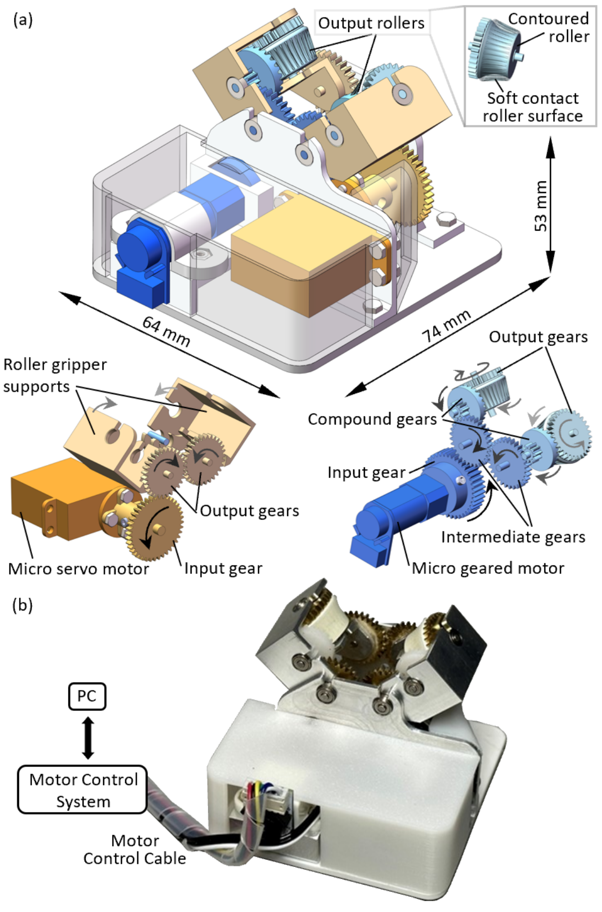

Fig. 6. FOB feeding module. (a) The mechanism design incorporates two gear transmission systems, highlighted in orange and blue, which facilitate the gripping and feeding functions respectively. (b) Compact module prototype.

$$\Delta x_a = -(\Delta x_b + \Delta l) \cdot \frac{E \cdot A}{(2k_1 + k_2)L + E \cdot A}, \tag{3}$$

and

$$F_{tension} = -(2k_1 + k_2)\Delta x_a. \tag{4}$$

The FOB distal end segment can be simplified as a series of rotational joints, allowing complex loads to be decomposed into non-degree-of-freedom directional loads and degree-of-freedom directional torques on the joints. Fig. 5(b) presents the deformation of the two tendons at the FOB distal end under the external torque T_x. Assuming the distal end follows the constant curvature assumption, with both tendons positioned along the outer side of the FOB and maintaining a constant distance d between them. Based on geometric properties that

$$\frac{l_1}{l_2} = \frac{r - d/2}{r + d/2}, \tag{5}$$

where r is the radius of the circular arc, l_1 and l_2 are the lengths of two tendons in the distal end, and

$$\Delta l_1 = -\Delta l_2 = -\frac{d \cdot l_0}{2r}, \tag{6}$$

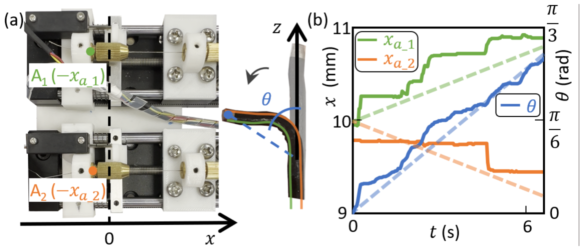

Fig. 7. Tendon stiffness self-modulation experiment of FOB tendons under bending. (a) Experimental setup for measuring driven unit displacements at constant overall FOB distal end stiffness. (b) Experimental results showing tendon stiffness self-modulation, with ideal results in dash line.

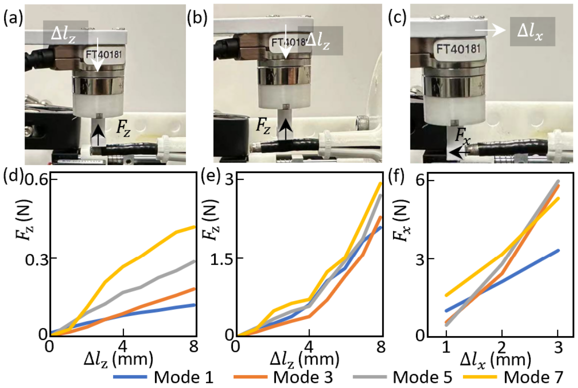

Fig. 8. FOB distal end self-modulation experiment in response to external influences. (a) Experimental setup of tip radial deformation and reactive force test. (b) Experimental setup of mid-tip radial deformation and reactive force test. (c) Experimental setup of tip compression deformation and reactive force test. (d)-(f) Results of (a)-(c) tests in different FOB distal end overall stiffness mode.

where $\Delta l_1 = l_1 - l_0$, and $\Delta l_2 = l_2 - l_0$ are differential displacements of two tendons in the distal end. Considering the interactions between the two tendons, we can derive

$$F_{tension1} - \Delta F_{torque} = F_{tension2} + \Delta F_{torque}, \tag{7}$$

where $\Delta F_{torque} = T_x/d$ is the reaction force to external torques T_x. Then, we get

$$\Delta x_{a1} - \Delta x_{a2} = -\frac{2T_x}{d(2k_1 + k_2)}, \tag{8}$$

$$\Delta l_1 = \frac{\Delta x_{b2} - \Delta x_{b1}}{2} + \frac{T_x((2k_1 + k_2)L + E \cdot A)}{d(2k_1 + k_2)E \cdot A}, \tag{9}$$

$$\Delta x_{a1} = -(\Delta x_{b1} + \Delta l_1) \cdot \frac{E \cdot A}{(2k_1 + k_2)L + E \cdot A}, \tag{10}$$

$$\Delta x_{a2} = -(\Delta x_{b2} - \Delta l_1) \cdot \frac{E \cdot A}{(2k_1 + k_2)L + E \cdot A}. \tag{11}$$

Thus, we get the FOB distal tip rotation radius of the circular arc and stiffness from the input x_{b1} and x_{b2}:

$$r = -\frac{d \cdot l_0}{2\Delta l_1}, \tag{12}$$

$$F_{tension1} = -(2k_1 + k_2)\Delta x_{a1} \tag{13}$$

$$F_{tension2} = -(2k_1 + k_2)\Delta x_{a2} \tag{14}$$

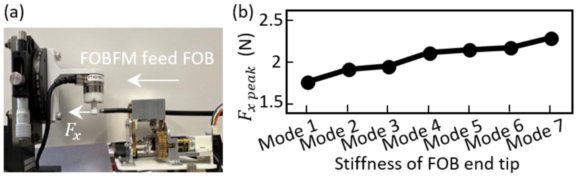

Fig. 9. Peak force experiment in FOBFM-fed FOB frontal impacts under various stiffnesses. (a) Experimental setup of FOBFM-fed FOB frontal impact. (b) Maximum peak frontal impact force results in 7 stiffness modes.

C. FOB Feeding Module (FOBFM)

To design a feed module capable of providing appropriate feeding force, we propose a compact FOB feed module as illustrated in Fig. 6(a). The module incorporates two sets of gear transmission mechanisms (shown in orange and blue). The orange one utilizes a micro servo motor (model ST-3032-C001) to generate precise angular motion, featuring a resolution of 0.088° and a rated torque of 0.15 Nm. This motion is transmitted via a gear train to actuate the roller gripper supports, inducing synchronous counter-rotation at equal angular velocities, thereby facilitating the gripping function. The blue one uses a micro-geared motor (model GM12N20) with a gear ratio of 1:210 to produce rotational motion. This motor offers a resolution of 0.25°, a rated torque of 0.08 Nm, and a nominal rotational speed of 130 rpm. A gear train that changes direction controls the output gears to rotate synchronously in opposite directions at the same speed, thereby facilitating the feeding function.

To facilitate fixation near the nasal cavity, it has compact dimensions of 74 × 64 × 53 mm and weighs 150 g. The output roller consisting of a contoured roller and a soft contact roller surface, optimized for intubation tasks. The output roller is 3D printed as an integrated unit using the Stratasys J826 3D Printer, with the soft surface made from a mixture of rubber-like photopolymer material with a Shore A hardness value of 30 and rigid photopolymer material, resulting in a material with a Shore A hardness value of 60. The feeding function is achieved through static friction between the soft surface and the controlled object, thus the maximum static friction force that the FOBFM can provide depends on the contact surface conditions and pressure.

III. EXPERIMENT

A. Variable-Stiffness FOBCM Dual Functionality Verification

To verify the model, we derive from Eqs. (9) to (14), especially for the tendon stiffness self-modulation mechanism. We fixed the driver units at the same place and acquired a constant overall FOB distal tip stiffness, as shown in Fig. 7(a). In this experiment, we set $\Delta x_{b1} = \Delta x_{b2} = \Delta x_b = 5$ mm. In an idealized model, we neglect frictional forces, assembly tolerances, and heterogeneities in tendon properties. The initial stiffness condition is $\Delta x_{a1_0} = \Delta x_{a2_0}$, in other words, $x_{a1_0} = x_{a2_0}$. From Eq. (6), we know $\Delta l_1 = -\Delta l_2 = -\frac{d \cdot l_0}{2r}$. And from Eq. (10), (11), (13), and (14), we can drive two linear relationships between Δx_{a1}, $F_{tension1}$, and Δl_1, and between Δx_{a2}, $F_{tension2}$, and Δl_2. Besides, based on geometric properties and the Eq. (12), we can drive a linear relationship between θ and Δl_1, $\theta = \frac{l_0}{2r} = -\frac{\Delta l_1}{d}$, where θ

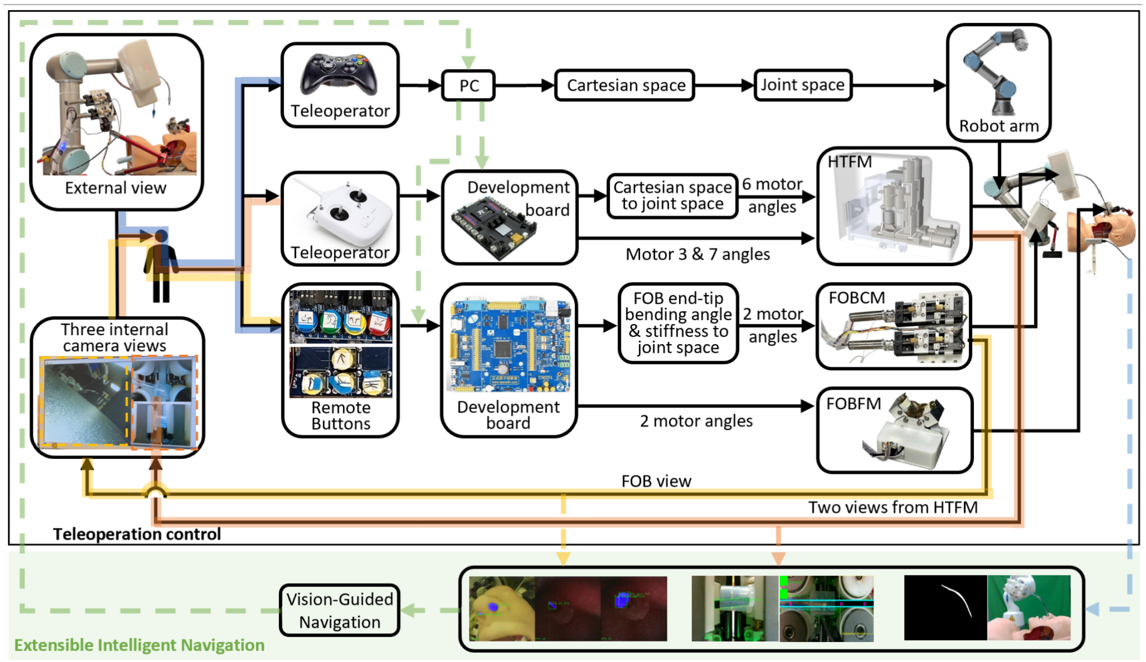

Fig. 10. Overall control architecture of the NIR system, with teleoperation control framework in black frame and potential extensible intelligent navigation in light green background.

represents the deflection angle of the FOB distal end, as shown in Fig. 7(a). Therefore, we can drive a linear relationship between Δx_{a1} and θ, Δx_{a2}, and θ:

$$\frac{d\Delta x_{a1}}{d\theta} = -\frac{d\Delta x_{a2}}{d\theta} = K, \tag{15}$$

where

$$K = \frac{E \cdot A \cdot d}{(2k_1 + k_2)L + E \cdot A}$$

denotes a coefficient related to the hardware setting.

The experimental results are shown in Fig. 7(b). As θ increases, x_{a1} increases linearly, while x_{a2} decreases, matching the theoretical model. x_{a2} exhibits steps due to significant movement resistance of the driven unit in module A_2 prototype. Additionally, initial position differences between x_{a1} and x_{a2} suggest longer initial tendon or screw length in module A_2 compared to A_1. Furthermore, opposing tendon movements during distal end positive bending generate opposite friction force, resulting in lower practical stiffness for A_2 and higher for A_1, causing a steeper slope for x_{a1} versus x_{a2}, which aligns with the experimental results.

To simulate the interaction between the FOB distal end and the environment under different overall stiffness conditions, FOB distal end self-modulation experiments were conducted in response to external influences. As shown in Fig. 8(a)-(c), three types of deformation and reactive force experiments were conducted: (a) tip radial deformation, (b) mid-tip radial deformation, and (c) tip axial compression. Experiment (a) & (b) were designed to simulate the bending self-modulation mechanism in response to lateral disturbances, while experiment (c) was designed to simulate the mechanism's behavior when subjected to frontal impacts in vivo.

A three-dimensional force sensor was used to record forces, with two sliding platforms independently controlling the sensor's translational movement in the x and z directions. After selecting a FOB distal end overall stiffness mode, we manually controlling the sensor's translation along the x or z axis, recording stable force readings at 1 mm intervals. Four distinct overall stiffness modes were tested for each experiment type, with Mode 1, 3, 5, and 7 corresponding to $\Delta x_{b1} = \Delta x_{b2}$ values of -1, 1, 3, and 5 mm, respectively. These values are driven by motor 1 and motor 2 through the rotation of the leadscrew.

Fig. 8(d)-(e) shows averaged results from three repetitions: low-stiffness modes (Modes 1 & 3) demonstrate buffering capability; high-stiffness modes (Modes 5 & 7) show load-bearing capacity. Tip lateral buffering capability is around 10 times that of mid-tip, and about 40 times that of frontal impact resistance. Specifically, for the conditions in Fig. 8(a)-(c), the lowest stiffness configuration, Mode 1, exhibits peak forces of 0.12 N, 2.0 N, and 2.8 N, whereas the highest stiffness configuration, Mode 7, demonstrates maximum reactive forces of 0.42 N, 2.9 N, and 4.9 N. Tip lateral buffering is positively correlating with stiffness. While for frontal impact resistance, the buffering capability exhibits more pronounced differences during the initial period. In summary, the experimental results reveal a notable variance in environmental interaction forces across the stiffness modes.

B. Passive Failure Protection Validation of FOBFM

The FOBFM exhibits passive failure protection characteristics due to the occurrence of slippage when the encountered resistance exceeds the maximum static friction. When feeding a FOB with an outer diameter of 4 mm, it can provide a maximum feeding force of 2 N, which means when the FOB is moving inside the body, it will immediately stop moving when the total resistance exceeds this value. And its maximum feeding speed is 90 mm/s. To evaluate the performance of

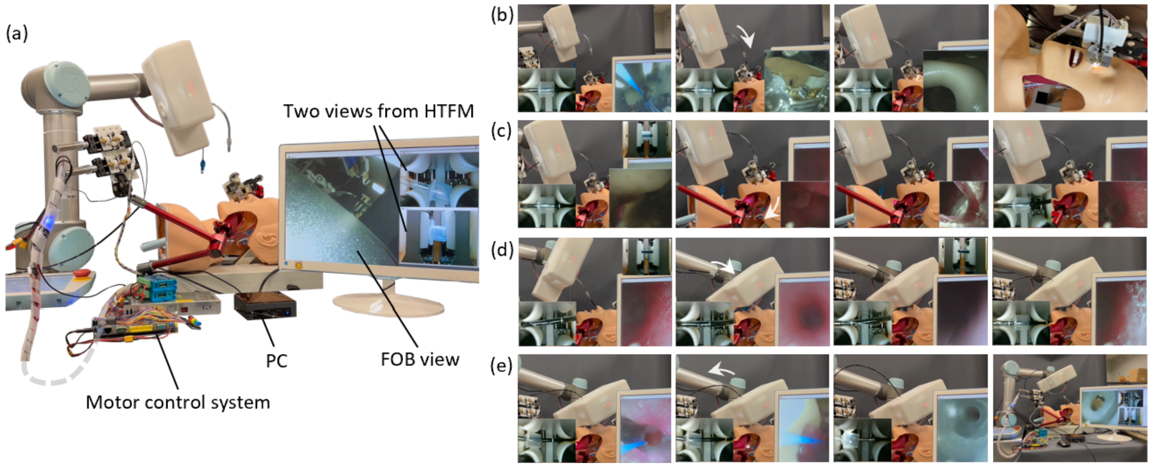

Fig. 11. Nasotracheal intubation application study in mannequin via teleoperation. (a) Experiment setup. (b) Initialization step: FOB pre-positioning near nostrils from the internal channel of NTT. (c) Step 1: FOB navigation through nasal passage to trachea. (d) Step 2: Proximal manipulation for NTT insertion along FOB. (e) Step 3: FOB withdrawal, NTT airway confirmation.

this mechanism under realistic conditions, we conducted peak force experiments on FOBFM-fed FOB frontal impacts across various stiffness configurations, as illustrated in Fig. 9(a). Specifically, utilizing FOBFM to feed FOB with randomly applied grip forces and maximum feeding speed under seven distinct stiffness modes, we executed frontal impacts more than five times on the three-dimensional force sensor along the x-axis. The maximum value among the impact force peaks was selected as the representative data for each mode. Fig. 9(b) shows the maximum peak impact forces across seven modes. Modes 1 through 7 correspond to $\Delta x_{b1} = \Delta x_{b2}$ values of -1, 0, 1, 2, 3, 4, and 5 mm, respectively. The results show a positive correlation between stiffness and peak impact force. Notably, in the highest stiffness configuration (Mode 7), the peak impact force exceeded the FOBFM's maximum static friction threshold of 2 N. This phenomenon can be attributed to the instantaneous dissipation of kinetic energy during collision. Conversely, low-stiffness modes facilitate rapid deformation upon impact, thereby attenuating the peak impact force. The experimental findings conclusively demonstrate that under FOBFM operation, FOB generates a maximum frontal impact force of 2.3 N with the help of a passive failure protection mechanism.

C. System Validation via Teleoperation

To validate the feasibility of the modular NIR system in nasotracheal intubation tasks, we employed a teleoperation approach to conduct coordinated testing of various system modules. The low-level control of each module, as illustrated in Fig. 3, 4(b), and 6(b), utilizes STM32-based development boards and can be controlled via teleoperator or remote buttons. The overall control architecture of the NIR system is shown in Fig. 10, wherein the operator analyzes external and three internal camera views to control HTFM, FOBCM, FOBFM, and the robotic arm. The low-level controller processes input control commands through kinematic model calculations to output direct control instructions for the motors.

As shown in Fig. 11(a), based on the aforementioned control architecture, we established an experimental setup to test the nasotracheal intubation application in a mannequin via teleoperation. Through the collaboration of multiple modules, the NTT is inserted into the trachea under FOB guidance, establishing an artificial airway for a mannequin. This process can be divided into the following steps, as illustrated in Fig. 11(b)-(e): 1) Use HTFM to control the FOB and NTT separately and move the FOB distal end near the nostril from the internal channel of NTT. 2) Mainly utilize FOBFD and FOBCD achieve FOB navigation through nasal passage to trachea with the help of FOB view. 3) Use HTFM, the NTT is inserted near the nostrils under FOB guidance. 4) FOB withdrawal is accomplished through HTFM manipulation, and the intubation's success can be validated from the FOB view. For a comprehensive demonstration of the procedure, please refer to the accompanying video supplement.

IV. CONCLUSIONS

This work presents a highly extensible modular robotic platform, the nasotracheal intubation robot, for nasotracheal intubation. The functionality is validated using teleoperation control on a mannequin. This system provides a hardware platform for others to advance nasotracheal intubation tasks at higher automation levels. Furthermore, this modular system can be expanded for applications in orotracheal intubation, automated medical endoscopy insertion, and industrial endoscopic inspection. We also introduced the FOBCM and FOBFM to manage the FOB. The variable-stiffness passive buffering mechanism in the FOBCM, combined with the passive failure protection mechanism in the FOBFM, limiting a maximum impact force of 2.3 N when the FOB unexpectedly encounters blockages or collisions inside the body. In the future, we can achieve rapid and stable intubation operations through intelligent navigation, and we can explore more ways to improve the first-attempt success rate of intubation. Additionally, we will continue to investigate the complex manipulation capabilities of the HTFM, utilizing its fine-tuning functions at the controlled object to complement the coarse adjustments of the robotic arm's end-effector.

REFERENCES

[1] W. W. Labaki and M. K. Han, "Chronic respiratory diseases: a global view," *The Lancet Respiratory Medicine*, vol. 8, no. 6, pp. 531–533, 2020.

[2] H. Wang, K. R. Paulson, S. A. Pease, S. Watson, H. Comfort, P. Zheng, A. Y. Aravkin, C. Bisignano, R. M. Barber, T. Alam *et al.*, "Estimating excess mortality due to the covid-19 pandemic: a systematic analysis of covid-19-related mortality, 2020–21," *The Lancet*, vol. 399, no. 10334, pp. 1513–1536, 2022.

[3] M. Urner, P. Jüni, B. Hansen, M. S. Wettstein, N. D. Ferguson, and E. Fan, "Time-varying intensity of mechanical ventilation and mortality in patients with acute respiratory failure: a registry-based, prospective cohort study," *The Lancet Respiratory Medicine*, vol. 8, no. 9, pp. 905–913, 2020.

[4] N. Murakami, R. Hayden, T. Hills, H. Al-Samkari, J. Casey, L. Del Sorbo, P. R. Lawler, M. E. Sise, and D. E. Leaf, "Therapeutic advances in covid-19," *Nature Reviews Nephrology*, vol. 19, no. 1, pp. 38–52, 2023.

[5] V. Russotto, S. N. Myatra, J. G. Laffey, E. Tassistro, L. Antolini, P. Bauer, J. B. Lascarrou, K. Szułdrzyński, L. Camporota, P. Pelosi *et al.*, "Intubation practices and adverse peri-intubation events in critically ill patients from 29 countries," *Jama*, vol. 325, no. 12, pp. 1164–1172, 2021.

[6] M. Bernhard, T. K. Becker, A. Gries, J. Knapp, and V. Wenzel, "The first shot is often the best shot: first-pass intubation success in emergency airway management," *Anesthesia & Analgesia*, vol. 121, no. 5, pp. 1389–1393, 2015.

[7] D. Obaseki, B. Adeniyi, T. Kolawole, C. Onyedum, and G. Erhabor, "Gaps in capacity for respiratory care in developing countries. nigeria as a case study," *Annals of the American Thoracic Society*, vol. 12, no. 4, pp. 591–598, 2015.

[8] J. Hansel, J. Law, N. Chrimes, A. Higgs, and T. Cook, "Clinical tests for confirming tracheal intubation or excluding oesophageal intubation: a diagnostic test accuracy systematic review and meta-analysis," *Anaesthesia*, vol. 78, no. 8, pp. 1020–1030, 2023.

[9] A. De Jong, A. Rolle, J. Pensier, M. Capdevila, and S. Jaber, "First-attempt success is associated with fewer complications related to intubation in the intensive care unit," *Intensive Care Medicine*, vol. 46, pp. 1278–1280, 2020.

[10] A. Gasmi Benahmed, A. Gasmi, W. Anzar, M. Arshad, and G. Bjørklund, "Improving safety in dental practices during the covid-19 pandemic," *Health and technology*, vol. 12, no. 1, pp. 205–214, 2022.

[11] S. Zhao, K. Ling, H. Yan, L. Zhong, X. Peng, S. Yao, J. Huang, and X. Chen, "Anesthetic management of patients with covid 19 infections during emergency procedures," *Journal of cardiothoracic and vascular anesthesia*, vol. 34, no. 5, pp. 1125–1131, 2020.

[12] P. E. Dupont, B. J. Nelson, M. Goldfarb, B. Hannaford, A. Menciassi, M. K. O'Malley, N. Simaan, P. Valdastri, and G.-Z. Yang, "A decade retrospective of medical robotics research from 2010 to 2020," *Science Robotics*, vol. 6, no. 60, p. eabi8017, 2021.

[13] H. Gao, Z. Zhang, C. Li, X. Xiao, L. Qiu, X. Yang, R. Hao, X. Zuo, Y. Li, and H. Ren, "Gesrsim: Gastrointestinal endoscopic surgical robot simulator," in *2022 IEEE/RSJ International Conference on Intelligent Robots and Systems (IROS)*. IEEE, 2022, pp. 9542–9549.

[14] H. Gao, R. Hao, X. Yang, C. Li, Z. Zhang, X. Zuo, Y. Li, and H. Ren, "Modeling and compensation of stiffness-dependent hysteresis for stiffness-tunable tendon-sheath mechanism in flexible endoscopic robots," *IEEE Transactions on Industrial Electronics*, 2023.

[15] C. Li, Y. Yan, X. Xiao, X. Gu, H. Gao, X. Duan, X. Zuo, Y. Li, and H. Ren, "A miniature manipulator with variable stiffness towards minimally invasive transluminal endoscopic surgery," *IEEE Robotics and Automation Letters*, vol. 6, no. 3, pp. 5541–5548, 2021.

[16] P. J. Tighe, S. Badiyan, I. Luria, S. Lampotang, and S. Parekattil, "Robot-assisted airway support: a simulated case," *Anesthesia and Analgesia*, vol. 111, no. 4, p. 929, 2010.

[17] T. Hemmerling, R. Taddei, M. Wehbe, C. Zaouter, S. Cyr, and J. Morse, "First robotic tracheal intubations in humans using the kepler intubation system," *British Journal of Anaesthesia*, vol. 108, no. 6, pp. 1011–1016, 2012.

[18] X. Wang, Y. Tao, X. Tao, J. Chen, Y. Jin, Z. Shan, J. Tan, Q. Cao, and T. Pan, "An original design of remote robot-assisted intubation system," *Scientific Reports*, vol. 8, no. 1, p. 13403, 2018.

[19] Z. Liang, H. Miao, Z. Guo, X. Zhu, X. Wang, Q. Cao, X. Tao, and T. Pan, "Pneumatic actuator based tracheal intubation system," in *Proceedings of 2020 3rd World Conference on Mechanical Engineering and Intelligent Manufacturing (WCMEIM)*, 2020, pp. 810–814.

[20] A. Cheng, Y. Qiu, H. Hao, Y. Xu, Y. Nie, Y. Jiang, X. Wu, Z. Guo, and G. Zheng, "Autonomous intubation robot system based on visual servoing and hybrid control," 2021.

[21] Q. Boehler, D. S. Gage, P. Hofmann, A. Gehring, C. Chautems, D. R. Spahn, P. Biro, and B. J. Nelson, "Realiti: A robotic endoscope automated via laryngeal imaging for tracheal intubation," *IEEE Transactions on Medical Robotics and Bionics*, vol. 2, no. 2, pp. 157–164, 2020.

[22] P. Biro, P. Hofmann, D. Gage, Q. Boehler, C. Chautems, J. Braun, D. R. Spahn, and B. Nelson, "Automated tracheal intubation in an airway manikin using a robotic endoscope: a proof of concept study," *Anaesthesia*, vol. 75, no. 7, pp. 881–886, 2020.

[23] G. Ponraj, C. J. Cai, and H. Ren, "Chip-less real-time wireless sensing of endotracheal intubation tubes by printing and mounting conformable antenna tag," *IEEE Robotics and Automation Letters*, vol. 7, no. 2, pp. 2369–2376, 2022.

[24] J. Lai, T.-A. Ren, W. Yue, S. Su, J. Y. Chan, and H. Ren, "Sim-to-real transfer of soft robotic navigation strategies that learns from the virtual eye-in-hand vision," *IEEE Transactions on Industrial Informatics*, 2023.

[25] G. Wang, T.-A. Ren, J. Lai, L. Bai, and H. Ren, "Domain adaptive sim-to-real segmentation of oropharyngeal organs," *Medical & Biological Engineering & Computing*, vol. 61, no. 10, pp. 2745–2755, 2023.

[26] Z. Deng, Y. Guo, S. Zhang, H. Jiang, X. Zheng, and B. He, "Development and image-guided control of a robotic endoscope system for nasotracheal intubation," *Mechatronics*, vol. 96, p. 103059, 2023.

[27] Z. Deng, S. Zhang, Y. Guo, H. Jiang, X. Zheng, and B. He, "Assisted teleoperation control of robotic endoscope with visual feedback for nasotracheal intubation," *Robotics and Autonomous Systems*, vol. 172, p. 104586, 2024.

[28] Z. Deng, P. Jiang, Y. Guo, S. Zhang, Y. Hu, X. Zheng, and B. He, "Safety-aware robotic steering of a flexible endoscope for nasotracheal intubation," *Biomedical Signal Processing and Control*, vol. 82, p. 104504, 2023.

[29] Z. Deng, X. Wei, X. Zheng, and B. He, "Automatic endoscopic navigation based on attention-based network for nasotracheal intubation," *Biomedical Signal Processing and Control*, vol. 86, p. 105035, 2023.

[30] Y. Guo, X. Wei, Z. Deng, X. Zheng, B. He, and J. Zhang, "Closed-loop robust control of robotic flexible endoscopy with neural network-based lumen segmentation," *Biomedical Signal Processing and Control*, vol. 86, p. 105340, 2023.

[31] X. Wei, Z. Deng, X. Zheng, B. He, and Y. Hu, "Weakly supervised glottis segmentation on endoscopic images with point supervision," *Biomedical Signal Processing and Control*, vol. 92, p. 106113, 2024.